Editors' Suggestion

Single-crystal growth and characterization of antiferromagnetically ordered $EuIn_2$

Brinda Kuthanazhi,[1,2] Simon X. M. Riberolles,[1,2] Dominic H. Ryan,[3] Philip J. Ryan,[4] Jong-Woo Kim,[4] Lin-Lin Wang,[1] Robert J. McQueeney,[1,2] Benjamin G. Ueland,[1,2] and Paul C. Canfield[1,2,*]

[1]*Ames National Laboratory, Iowa State University, Ames, Iowa 50011, USA*

[2]*Department of Physics and Astronomy, Iowa State University, Ames, Iowa 50011, USA*

[3]*Department of Physics, McGill University, Montreal, Québec H3A 2T8, Canada*

[4]*Advanced Photon Source, Argonne National Laboratory, Argonne, Illinois 60439, USA*

(Received 7 August 2023; revised 22 January 2024; accepted 29 April 2024; published 3 June 2024)

We report the single-crystal growth and characterization of $EuIn_2$, a magnetic topological semimetal candidate, according to our density functional theory (DFT) calculations. We present results from electrical resistance, magnetization, Mössbauer spectroscopy, and x-ray resonant magnetic scattering (XRMS) measurements. We observe three magnetic transitions at $T_{N1} \sim 14.2$ K, $T_{N2} \sim 12.8$ K, and $T_{N3} \sim 11$ K, signatures of which are consistently seen in anisotropic temperature-dependent magnetic susceptibility and electrical resistance data. Mössbauer spectroscopy measurements on ground crystals are consistent with an incommensurate sinusoidally modulated magnetic structure below the transition at $T_{N1} \sim 14$ K, followed by the appearance of higher harmonics in the modulation on further cooling roughly below $T_{N2} \sim 13$ K before the moment distribution squaring up below the lowest transition around $T_{N3} \sim 11$ K. XRMS measurements showed the appearance of magnetic Bragg peaks below $T_{N1} \sim 14$ K, with a propagation vector of $\boldsymbol{\tau} = (\tau_h, \bar{\tau}_h, 0)$, with τ_h varying with temperature, and showing a jump at $T_{N3} \sim 11$ K. The temperature dependence of τ_h between ~11 and 14 K shows incommensurate values consistent with the Mössbauer data. XRMS data indicate that τ_h remains incommensurate at low temperatures and locks into $\tau_h = 0.3443(1)$.

DOI: 10.1103/PhysRevB.109.214401

I. INTRODUCTION

The search for new topological materials and an understanding of their physics has driven new materials physics research in the last few years [1–8]. Whereas the predicted topological properties are not always observed, the search has lead to the discovery of fascinating magnetic structures and prompted research into understanding the microscopic interactions controlling the magnetic ordering [9–13]. In magnetic Weyl semimetals, magnetism coexists with and modifies the nontrivial topology of the electronic bands of the material by breaking symmetries. This is achieved by either providing a wave vector associated with a low temperature antiferromagnetic (AFM) state or imposing a long-range internal field via adopting a state with a ferromagnetic (FM) component.

Divalent Eu-containing binary and ternary compounds have become fertile grounds for looking for magnetic Weyl semimetal candidates. [11,14–18] In its 2+ valence, europium is magnetic with an effective angular momentum $J = S + L = 7/2$ that is fully associated with the electron spin $S = 7/2$, with L being zero. In many cases, magnetism can be tuned by various parameters such as chemical doping [16], hydrostatic pressure [19], and uniaxial strain.

The rich phase space of complicated magnetic states provided by Eu^{2+} containing compounds has contributed to our understanding of competing magnetic interactions, magnetic frustration, helical magnets, etc. [11,20,21]. However, precisely determining the magnetic structure of divalent Eu containing compounds through neutron diffraction studies remains extremely challenging due to the high thermal neutron absorption of Eu. In this study, we use a complementary set of techniques, including single crystal anisotropic magnetization measurements, ^{151}Eu Mössbauer spectroscopy, and x-ray resonant magnetic scattering to gain information about the magnetic phases in $EuIn_2$ which shows multiple phase transitions.

Recently, a theoretical study predicted $EuTl_2$ would host a variety of topological phases depending on the strength of the magnetic interactions, as well as by varying strain [18] $EuTl_2$ forms in the $CaIn_2$ structure type with the hexagonal structure in space group $P6_3/mmc$ (No. 194). [22] $EuIn_2$, which is much more amenable to growths than the toxic and volatile Tl, crystallizes in the same $CaIn_2$ structure and could therefore be another possible candidate for various topological phases. In the literature, $EuIn_2$ was synthesized in polycrystalline form and magnetic measurements were only done for temperatures above ~100 K [22,23]. However, no reports exist about the low-temperature behavior of this compound. Therefore the nature or even existence of magnetic order is unknown. As such $EuIn_2$ is a compound that merits further investigation.

Here, we report the results of DFT calculations on $EuIn_2$, predicting the existence of Dirac points in the nonmagnetic state, which makes it a candidate for a magnetic topological semimetal if magnetic ordering can be confirmed

*canfield@ameslab.gov

and delineated. We report the single-crystal synthesis, electrical transport measurements, and magnetic characterization of $EuIn_2$. We find signatures of three magnetic ordering temperatures at $T_{N1} \sim 14.2$ K, $T_{N2} \sim 12.8$ K and $T_{N3} \sim 11$ K in temperature dependent magnetization and electrical resistance measurements. Further measurements by Mössbauer spectroscopy and x-ray resonant magnetic scattering results provide insight into the nature of the magnetic ordering occurring below these temperatures. Taken together, our results indicate that $EuIn_2$ exhibits intriguing closely lying antiferromagnetic phases with a temperature-dependent incommensurate AFM propagation vector.

II. EXPERIMENTAL AND COMPUTATIONAL METHODS

Single crystals of $EuIn_2$ were grown out of excess In using the high-temperature solution growth method [24–26]. Elements (Eu - Ames Laboratory, 99.99+ % and In - Alfa Aesar, 99.999%) with an initial stoichiometry of $Eu_{15}In_{85}$ were weighed out into a fritted alumina crucible set (Canfield Crucible Set) [25] and sealed in a fused silica tube with a partial pressure (1/4 atm) of argon. The prepared ampoule was then heated up to 800 °C over 4 hours and held there for 3 hours. This was followed by a slow cooling to 480 °C over 50 hours and decanting the excess flux using a centrifuge [24,26]. The choice of decanting temperature at 480 °C is to avoid the possible formation of $EuIn_4$ below the 450 °C peritectic line (ASM Diagram No. 901007 [27]). The crystals obtained had a hexagonal morphology and were air sensitive, with the surface turning white/oxidized within about 15 minutes of exposure to air. They were stored and handled inside a nitrogen filled glovebox.

Powder x-ray diffraction measurements were carried out at ambient temperature to determine the phase purity. The powder x-ray diffraction pattern was collected on ground crystals using a Rigaku Miniflex diffractometer inside a nitrogen filled glovebox, with Cu K_α radiation. Crystallographic parameters were obtained from a Rietveld refinement using GSAS-II software [28].

The magnetic measurements were carried out in a Quantum Design Magnetic Property Measurement System with applied fields up to 70 kOe. A single-crystal sample was mounted on a poly-chloro-tri-fluoro-ethylene disk using super glue, and the separately measured background of the disk was subtracted. The contribution of glue to magnetization is neglected. The same crystal and mounting were used for measurements in both directions. No corrections or subtraction of core diamagnetism were applied. The order of magnetic measurements was as follows. At first the in-plane applied field $M(H)$ measurement with increasing and decreasing fields was carried out at 2 K. Then the sample was warmed to 30 K above all transitions at zero field. This was followed by cooling to 1.8 K at zero field. Then, a zero field cooled $M(T)$ on warming and field cooled $M(T)$ on cooling at 100 Oe was measured. The 1 kOe $M(T)$ measurement on warming to 300 K followed. The same protocol was followed for $H \parallel c$ measurements after this. The field was set to zero each time in the "oscillating" mode in the MPMS, to minimize the remnant field.

The AC resistivity measurements were done in a Quantum Design Physical Property Measurement System in the standard four point configuration. The current along the c axis was $I = 3$ mA at a frequency of $f = 17$ Hz. Contacts were made using Dupont-4929N silver paint.

The ^{151}Eu Mössbauer spectroscopy measurements were carried out on ground samples of $EuIn_2$, using a 3 GBq $^{151}SmF_3$ source, driven in sine-mode and calibrated using a standard ^{57}Co Rh/α-Fe foil. Isomer shifts are quoted relative to EuF_3 at ambient temperature. A linewidth of 1.25(2)mm/s (HWHM) is observed with the standard. The sample was hand-ground under hexane (to minimise oxidation) and mixed with boron nitride before being loaded into a thin-window delrin sample holder. The sample was cooled in a vibration-isolated closed-cycle helium refrigerator with the sample in helium exchange gas. The spectra taken below 10 K and above 15 K could be fitted conventionally using a sum of Lorentzian lines with the positions and intensities derived from a full solution to the nuclear Hamiltonian [29]. However, spectra taken in the incommensurate modulated phase between 10 and 15 K (see discussions below) were fitted using a model that derives a distribution of hyperfine fields from an (assumed) incommensurate sinusoidally modulated magnetic structure [30,31].

X-ray resonant magnetic scattering measurements were obtained at end station 6-ID-B at the Advanced Photon Source, Argonne National Laboratory, for the Eu L_2 edge ($E = 7.617$ keV [32]) using the Huber Psi-circle geometry diffractometer. An approximately 0.5 mm thick single-crystal with a cross section of ≈1 mm × 1 mm was mounted on a Cu sample holder with carbon tape, and the holder was thermally anchored to the cold head of a He displex with the **c** crystalline axis horizontal. Care was taken to minimize the exposure time of the sample to air. The instrument was operated in vertical geometry, allowing access to several $(h\,k\,l)$ reciprocal-lattice points. Incident x-rays were linearly polarized perpendicular to the vertical scattering plane (σ polarized), and no polarization analysis of the diffracted beam was performed. A two-dimensional Pilatus 100 K detector was employed, the incident beam size was 0.248 mm × 0.600 mm (height by width). An attenuator with a calculated transmission of 0.396564 was used when recording the data shown below in order to mitigate beam heating of the sample. Nevertheless, a comparison of the XRMS data with the thermodynamic, transport, and Mössbauer spectroscopy data indicated a $T \approx 1$ K difference in features in the data, presumably due to beam heating leading to the sample being slightly warmer than the recorded temperature. We have therefore shifted the XRMS data points up by 1 K above the temperature reported by the instrument thermometry.

Band structures of nonmagnetically ordered $EuIn_2$ have been calculated without Eu $4f$ orbitals in density functional theory [33,34] using PBE [35] as exchange-correlation functional with spin-orbit coupling (SOC) effect included. All DFT calculations have been performed in VASP [36,37] with a plane-wave basis set and projector augmented wave [38] method. We used the hexagonal unit cell of 6 atoms with a Γ-centered Monkhorst-Pack [39] (10 × 10 × 6) k-point mesh with a Gaussian smearing of 0.05 eV. The kinetic energy cutoff was 400 eV.

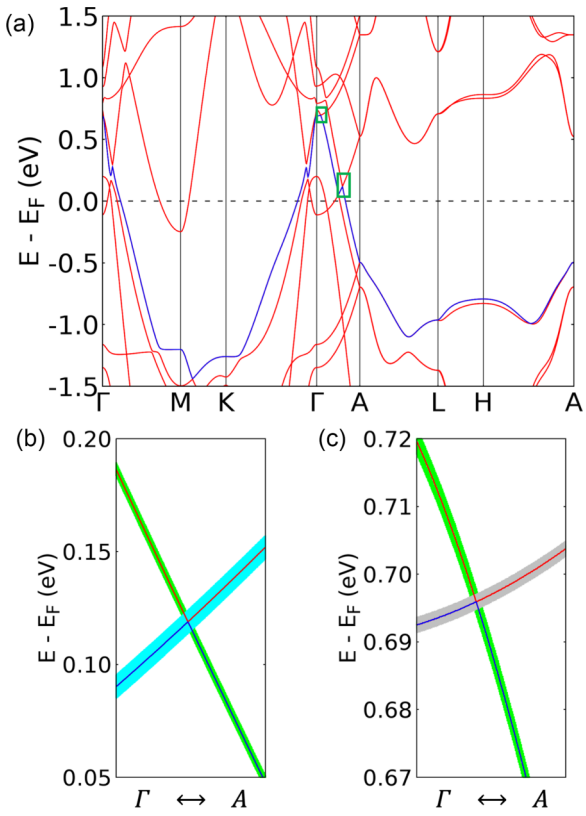

FIG. 1. (a) Bulk band structure of nonmagnetically ordered $EuIn_2$ calculated in PBE + SOC without Eu 4f orbitals. Green rectangles mark the region that is shown in (b) and (c), zooming in near the two Dirac points along the Γ-*A* direction. The top valence band is in blue. The green, cyan and grey shades stand for the projection of In p_y, In *s* and Eu d_{yz} orbitals, respectively.

III. RESULTS AND DISCUSSION

A. DFT results

Our experimental study was largely motivated by our DFT calculations revealing the potential presence of topological fermions which could be influenced by magnetic ordering. The bulk band structure of nonmagnetically ordered $EuIn_2$, without Eu 4*f* orbitals, is plotted in Fig. 1(a) with the highest valence band in blue according to simple filling. The valence and conduction bands are generally well removed from the Fermi level E_F over most of the Brillouin zone except for an electron pocket at the *M* point and the overlap between valence and conduction bands around the Γ point. Especially along the Γ-*A* direction, there are two gapless crossing points between the top valence and bottom conduction bands protected by the threefold rotational symmetry, i.e., Dirac points. As zoomed in Figs. 1(b) and 1(c), these two Dirac points are above E_F and have the momentum energy of (0, 0, ±0.24 $Å^{-1}$; $E_F + 0.12$ eV) and (0, 0, ±0.04 $Å^{-1}$; $E_F + 0.70$ eV), respectively. The lower Dirac point has a switch of orbital character between In p_y and In *s*, whereas the upper Dirac point is between In p_y and Eu d_{yz}. Similar to $EuTl_2$ [18], these Dirac points can act as the parent gapless phase to be transformed into different descendent phases, depending on the existence and nature of magnetic ordering. As such, it is of interest to know what type of magnetic structures $EuIn_2$ hosts.

B. Powder x-ray diffraction, resistivity, and magnetization

The powder x-ray diffraction pattern shown in Fig. 2(a) confirms the $P6_3/mmc$ structure of $EuIn_2$, with lattice parameters $a = 4.9814(2)$ Å and $c = 7.8713(2)$ Å obtained from Rietveld refinement (with a weighted *R* factor $wR = 5.08\%$

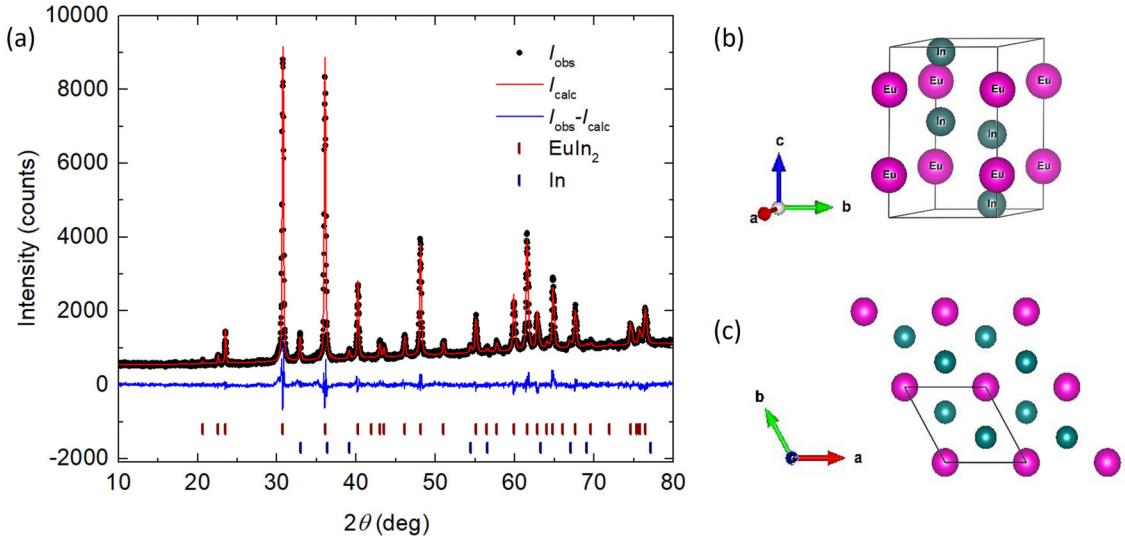

FIG. 2. (a) Room temperature powder x-ray diffraction pattern with Rietveld refinement of $EuIn_2$, in the space group $P6_3/mmc$, with lattice parameters $a = 4.9814(2)$ Å and $c = 7.8713(2)$ Å. The black points show the observed scattering intensity, the red line shows the calculated pattern and the blue line shows the difference between the two. The red and blue bars show the Bragg peak positions for $EuIn_2$ and In, respectively. (b) Crystal structure of $EuIn_2$. (c) Projection of the structure along the crystallographic *c* axis, showing the triangular lattice of magnetic Eu^{2+} ions.

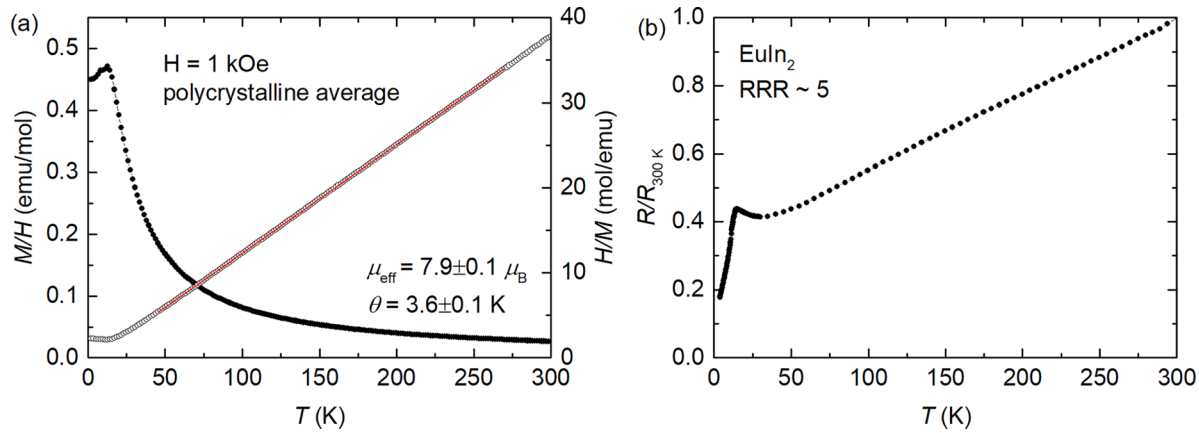

FIG. 3. (a) Polycrystalline average of the magnetic susceptibility $M(T)/H$ along with the right y axis showing the inverse susceptibility $H/M(T)$, with the linear fit (red line between 50 and 250 K) showing the Curie-Weiss behavior. (b) Normalized electrical resistance $R/R_{300\,\mathrm{K}}$ as a function of temperature. RRR is the residual resistivity ratio given by $R(300\,\mathrm{K})/R(2\,\mathrm{K})$. All data below $T = 3.5$ K were removed as small amounts of remnant In flux present become superconducting below this temperature.

and goodness of fit of 1.58 - see Table I below). Some impurity peaks are present, which can be identified as In, with about 6% phase fraction of In present. Given that the $EuIn_2$ is grown out of an excess of In, this is the expected impurity. The In most likely comes from small droplets of solidified, excess liquid that adhered to the $EuIn_2$ crystals through the decanting step. Lattice parameters obtained from Rietveld refinement agree with the existing report. [22] Table I in the Appendix shows the other parameters from the Rietveld refinement. Figure 2(b) shows the three dimensional crystal structure of $EuIn_2$, and (c) shows the projection along the c axis. The Eu^{2+} ions form a triangular lattice in the ab plane, a geometry conducive to magnetic frustration.

We first survey the temperature dependence of $M(T)$ and $R(T)$ over a wide temperature range (300 K $> T >$ 3.5 K). The low-field magnetization data and the resistivity data shown in Fig. 3 and Fig. 4 are truncated at $T = 3.5$ K as the In flux present becomes superconducting below this temperature, which gives rise to small discontinuities. The polycrystalline average of the magnetic susceptibility was obtained using $(M/H)_{\mathrm{poly}} = \frac{1}{3}(M/H)_{\mathrm{parallel}} + \frac{2}{3}(M/H)_{\mathrm{perp}}$, where the subscripts 'parallel' and 'perp' denote the applied field directions $H||c$ and $H \perp c$ respectively. Figure 3(a) shows the polycrystalline average of M/H plotted as a function of temperature for an applied field of $H = 1$ kOe. The high-temperature region shows a Curie-Weiss behavior. The right-hand axis of Fig. 3(a) shows the inverse susceptibility with a linear fit. The fitting parameters of the linear fit gave an effective moment of $\mu_{\mathrm{eff}} = 7.9 \pm 0.1\mu_B$ (consistent with the 7.94 μ_B theoretically anticipated for Eu^{2+}) and $\theta = 3.6 \pm 0.1$ K. A small positive θ is obtained, indicating a ferromagnetic interaction, but with a value less than half of the transition temperature, indicating possible competing AFM and FM interactions. Invoking the existence of competing magnetic interactions is further justified by multiple closely spaced magnetic transitions observed, as discussed below. Normalized electrical resistance $R/R_{300\,\mathrm{K}}$ is plotted in Fig. 3(b). The sample has a residual resistivity ratio of ≈ 5. The low-temperature resistivity shows a slight upturn followed by a sharp decrease due to loss of spin disorder scattering at ≈ 15 K, which is consistent

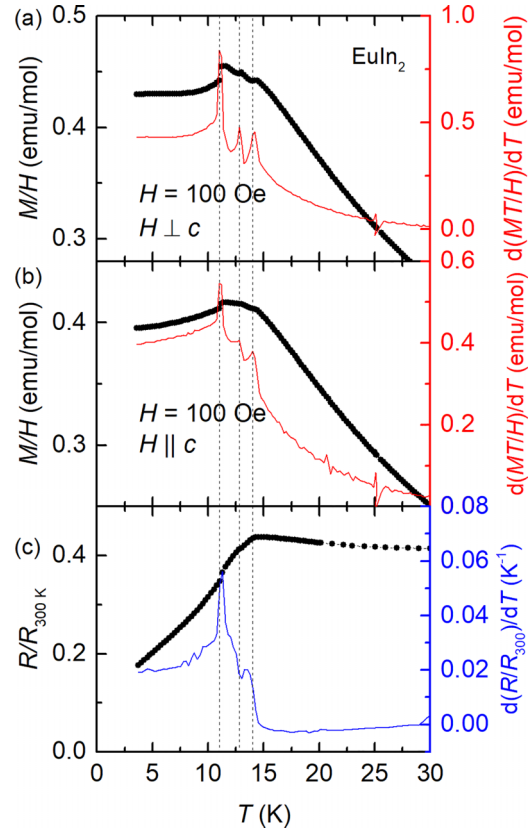

FIG. 4. Magnetic susceptibility $M(T)/H$ of $EuIn_2$ and the temperature derivative $d(MT/H)/dT$ as a function of T, for an applied field of $H = 100$ Oe with (a) $H \perp c$. (b) $H \parallel c$. (c) Normalized resistance $R/R_{300\,\mathrm{K}}$ and the temperature derivative of it $d(R/R_{300\,\mathrm{K}})/dT$. The data below $T = 3.5$ K are removed as the In flux present becomes superconducting below this temperature. The three vertical dashed lines indicate the temperature values of local maxima in $d(MT/H)/dT$ and cross through $d(R/R_{300\,\mathrm{K}})/dT$ data near maximum local slope points.

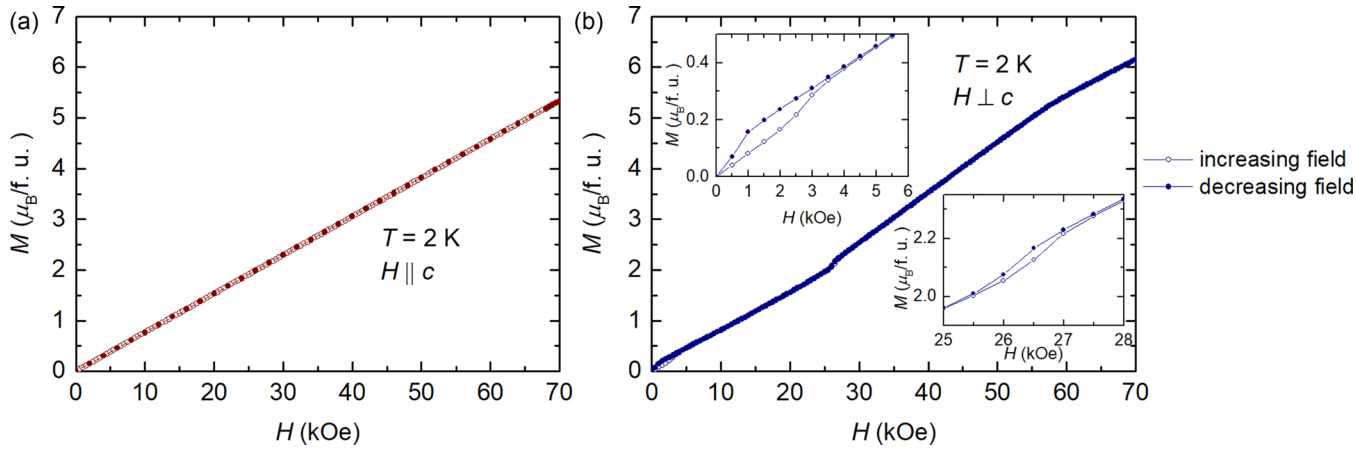

FIG. 5. Magnetization as a function of applied field, $M(H)$, of $EuIn_2$ for fields up to 70 kOe, measured at $T = 2$ K, with the field directions (a) $H \parallel c$ and (b) $H \perp c$. Insets show the zoom-in of the field regions close to $H = 1$ and 26 kOe, showing the hysteretic nature of the two transitions. The open and closed symbols denote increasing and decreasing field measurements, respectively.

with a magnetic ordering transition. We see signatures of up to three transitions in the magnetization data between 10−15 K. These can be clearly seen in the anisotropic magnetic susceptibilities, resistivity, and their derivatives, shown in Fig. 4. Figure 4(a) shows magnetic susceptibility M/H, measured under field cooling, and the temperature derivative $d(MT/H)/dT$ [40] as a function of T, for an applied field of $H = 100$ Oe, with $H \perp c$. Similar data for $H \parallel c$ are shown in Fig. 4(b). Figure 4(c) shows the normalized resistance $R/R_{300\,\mathrm{K}}$ and its temperature derivative, $d(R/R_{300\,\mathrm{K}})/dT$, [41] on the right y axis. The signatures of three transitions are seen in the derivatives of both $M(T)/H$ data sets, with transition temperatures of $T_{N1} = 14.2 \pm 0.2$, $T_{N2} = 12.8 \pm 0.2$, and $T_{N3} = 11.0 \pm 0.2$K. Similar transition temperatures can be inferred from the dR/dT data. Whereas the two higher temperature transitions have features consistent with second-order phase transitions, the more discontinuous nature of the $M(T)$ and $R(T)$ data for the lowest temperature transition, along with the shape of the derivative curves, suggest that $T_{N3} \sim 11$ K may be associated with a first-order phase transition.

Magnetization as a function of field $M(H)$ data for $T = 2$ K are shown in Fig. 5(a) for $H \parallel c$ and Fig. 5(b) for $H \perp c$. Superconducting indium has a critical field of $H_c \sim 250$ Oe, at $T \sim 1$ K [42], so the effects on $M(H)$ data are minimal. Also, In features would be isotropic because the In is primarily in the form of tiny polycrystalline droplets or streaks adhering to the surface of the crystal. The measurement was done by cooling the sample to 2 K in zero field and then measuring while increasing and decreasing the magnetic field. The $H \parallel c$ data show linear behavior, with increasing and decreasing fields overlapping. In contrast, $M(H)$ for $H \perp c$ shows subtle features corresponding to various possible spin re-orientation transitions. There is a low field, hysteretic transition between 1–3 kOe, shown more clearly in the inset of Fig. 5(b). There are also two more subtle features in $M(H)$: one around 27 kOe that also shows a small hysteresis [second inset of Fig. 5(b)], and another change of slope around 57 kOe where no discernible hysteresis was observed. While subtle, all three features were noted in measurements of several distinct samples and are therefore belived to be intrinsic to $EuIn_2$.

C. Mössbauer spectroscopy

Figure 6 shows ^{151}Eu Mössbauer spectra for $EuIn_2$ taken at representative, low temperatures. At 14 K, a single line corresponding to Eu^{2+} close to −10 mm/s is observed. A ∼5% Eu^{3+} impurity is also apparent as the weak absorption at ∼0 mm/s, an impurity that may result from some of the sample being oxidized, and this was included in all of the fits. As the temperature decreases through 14 K the spectrum broadens and splits, marking the development of magnetic order. Between 13 and 11 K, the two inner lines have higher intensities than the outer ones, leading to a spectral shape with

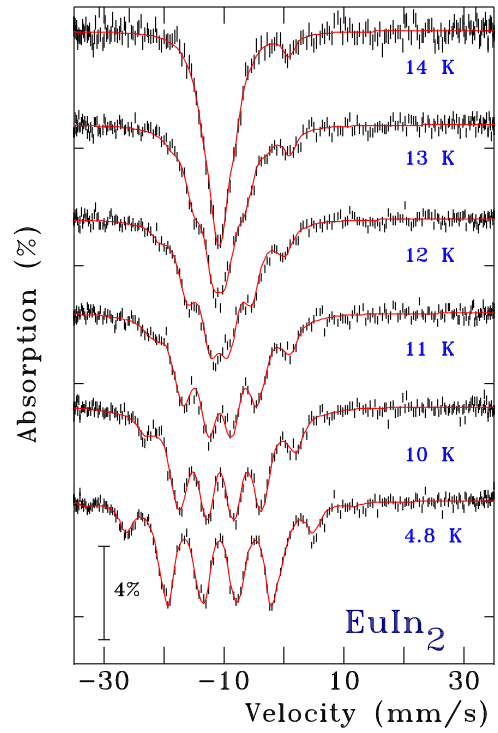

FIG. 6. ^{151}Eu Mössbauer spectra of $EuIn_2$ at various temperatures as we cool down from 14 to 4.8 K. The red solid lines are fit using the modulated model explained in the text.

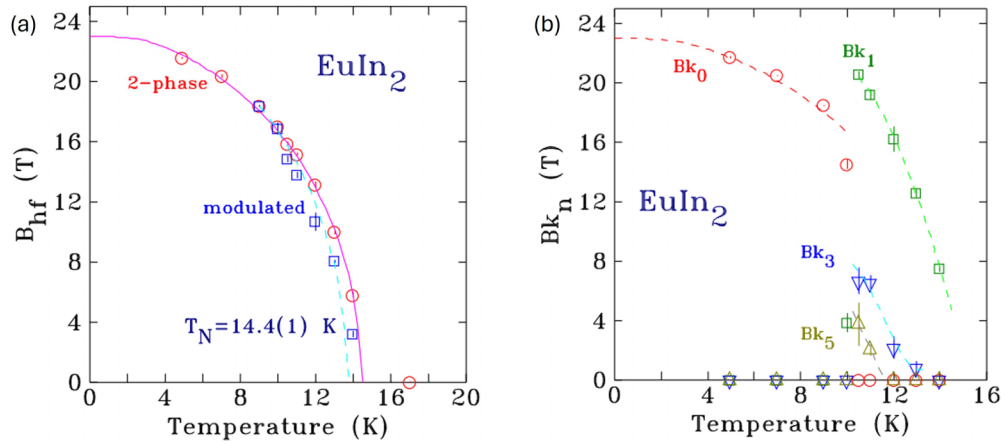

FIG. 7. (a) Temperature dependence of the hyperfine field $B_{\rm hf}$ obtained from fitting the Mössbauer spectra using a two-component fit for $EuIn_2$ shown in red circles. The temperature dependence of the average hyperfine field from the modulated fit is shown in blue square symbols. (b) Temperature variations of the Fourier components of the hyperfine field from fitting the Mössbauer spectra using a modulated model.

more weight in the center. As $EuIn_2$ is cooled further to 4.8 K, the spectra show a well-split magnetic pattern, with a hyperfine field ($B_{\rm hf}$) of 21.5(1) T and isomer shift of −10.74(3) mm/s, values typical for a magnetically ordered Eu^{2+} compound [43] (Fig. 6 bottom spectrum). No information on the ordering direction within the crystallographic cell can be obtained from this spectrum as the observed quadrupole contribution, 0.0(3) mm/s, is consistent with zero. The spectra between 11 and 13 K, with the rapidly growing central area, can be modeled by a simple two-component fit, one magnetic with a temperature-dependent $B_{\rm hf}$, and the other with no magnetic splitting. However, this gives unphysical results with a large nonmagnetic component and increasing linewidths (see Appendix B for more details). Despite this, fitting the derived $B_{\rm hf}$(T) using a $J = \frac{7}{2}$ Brillouin function provides an estimated ordering temperature of 14.4(1) K, consistent with $T_{\rm N1}$, as shown in Fig. 7(a). The observed spectral shape can also be fitted by a more physically likely model, with a distribution of hyperfine fields resulting from incommensurate modulation of moments [30], as has been observed in many other Eu^{2+} compounds. [20,31,44]

In order to fit the data using the modulated model, we first assume that the moment modulation along the direction of the propagation vector **k** can be written in terms of its Fourier components. We further assume that the observed hyperfine field is a linear function of the Eu^{2+} moment at any given site. Then the variation of $B_{\rm hf}$ with distance x along the propagation vector **k** can be written as [30]

$$B_{\rm hf}(kx) = Bk_0 + \sum_{l=0}^{\infty} Bk_{2l+1} \sin(2l+1)kx, \qquad (1)$$

where the Bk_n (with $n = 2l + 1$) are the odd Fourier coefficients of the field modulation. As $+B_{\rm hf}$ and $-B_{\rm hf}$ are indistinguishable, kx only needs to run over half the modulation period, and in this case, an incommensurate square-wave structure can be modeled either as a sum over a very large number of Fourier coefficients or by simply using the Bk_0 term with all of the other Bk_n set to zero. We found the fits to be far more stable with the Bk_0 term included rather than using a large set of Bk_n; however, the two approaches are effectively equivalent. Variations of this model have also been used to fit spectra of EuPdSb [30] and Eu_4PdMg [45].

Adopting the incommensurate modulated model to analyze the spectra yields the fits shown in Fig. 6, and the temperature dependence of the derived modulation harmonics is shown in Fig. 7(b). The protocol for fitting is given in more detail in Appendix B. Starting from the lowest temperature, we see that only Bk_0 is present in the 4.8 K spectrum. This suggests that the ground state is a squared-up state without moment modulations, i.e., all of the europium moments have the same magnitude. We emphasise that this *does not* indicate that this ordering is commensurate, as we are blind to any variations in moment direction due to the absence of a quadrupole contribution noted above. On warming above $T_{\rm N3}$, the higher harmonics Bk_1, Bk_3, and Bk_5 appear, indicating the development of a modulated structure. With further warming, the higher harmonic contributions become weaker, and only Bk_1 survives, indicating that the order evolves towards a purely sinusoidally modulated state before disappearing at ∼14 K.

Thus the Mössbauer results suggest that $T_{\rm N1}$ at ∼14 K is a transition to an incommensurate antiferromagnetic state. $T_{\rm N2}$ at ∼13 K might be associated with the start of the process of higher harmonics developing in the modulated order, and $T_{\rm N3}$ at ∼11 K marks the completion of the squaring up of the moment modulation leading to all of the europium moments being equal. Further insight into the microscopic details of the Eu^{2+} ordering requires magnetic scattering measurements.

D. X-ray resonant magnetic scattering

We used XRMS to determine the magnetic propagation vectors associated with the multiple magnetic phases below 14 K. Data from the scans described below determined the existence of an antiferromagnetic propagation vector of $\boldsymbol{\tau} = (\tau_h, \bar{\tau}_h, 0)$. As explained earlier, all XRMS data discussed below are presented with the temperature shifted higher by 1 K, to account for the beam heating. This makes the features seen in XRMS coincide well with those from Mössbauer spectroscopy, magnetization and resistance measurements.

X-ray energy scans across the Eu L_2 edge were taken at $T = 5$ and 21 K after aligning to the $(2 + \tau_h, \bar{\tau}_h, 2)$ magnetic-

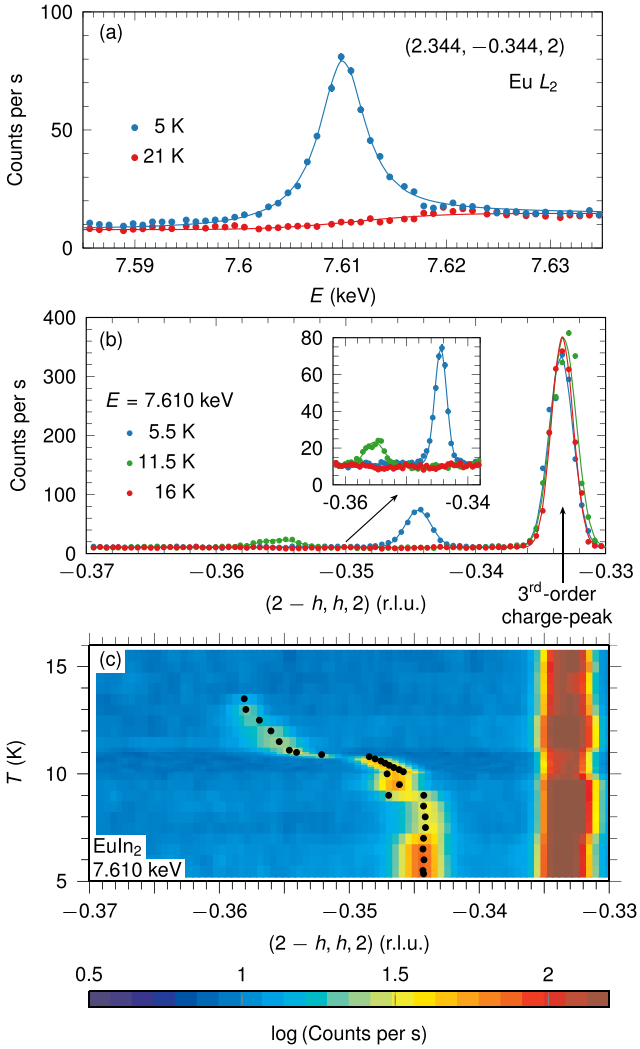

FIG. 8. (a) X-ray energy scan across the Eu L_2 edge for $(2+\tau_h, \bar{\tau}_h, 2)$ at 21 and 5 K. (b) Diffraction patterns across the $(2+\tau_h, \bar{\tau}_h, 2)$ magnetic-Bragg peak using 7.610 keV x rays at 5.5, 11.5, and 16 K. As explained in the text, the peak at $(2\frac{1}{3}, -\frac{1}{3}, 2)$ is due to the $(7, \bar{1}, 6)$ structural-Bragg peak. (c) Image plot showing a detailed temperature dependence of the $(2+\tau_h, \bar{\tau}_h, 2)$ magnetic-Bragg peak from 7.610 keV XRMS data. Black dots mark the centers of the magnetic-Bragg peak as determined from fits to Gaussian line shapes. Error bars are smaller than the symbol size if they are not visible. All temperatures presented are increased by 1 K, as discussed in the text.

Bragg peak of our single-crystal sample at 5 K and are shown in Fig. 8(a). A large resonant enhancement is seen just below the absorption edge around $E = 7.610$ keV for 5 K but not for 21 K. This is consistent with an enhancement of dipole transitions of $2p$ core-level electrons to empty $5d$ states due to the presence of magnetic order at 5 K. Based on these data, we made a series of longitudinal, rocking, and other reciprocal-space scans using 7.610 keV x-rays to characterize the temperature dependence of the magnetic-Bragg peaks. Figures 8(b) and 8(c) summarize the main results.

Figure 8(b) shows data from scans along $(2-h, h, 2)$ at different temperatures. The $(2+\tau_h, \bar{\tau}_h, 2)$ magnetic-Bragg

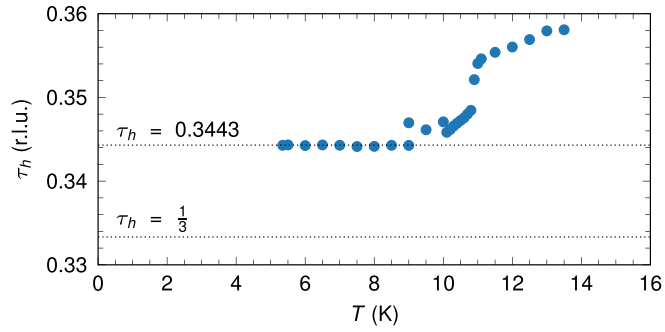

FIG. 9. The temperature dependence of τ_h, the component of the three symmetry equivalent antiferromagnetic propagation vectors $\boldsymbol{\tau} = (\tau_h, 0, 0)$, $(0, \tau_h, 0)$, and $(\bar{\tau}_h, \tau_h, 0)$ determined from XRMS measurements of the $(2+\tau_h, \bar{\tau}_h, 2)$ magnetic-Bragg peak of a single-crystal sample. The temperatures presented are are increased by 1 K, as discussed in the text.

peak is visible for $T = 5.5$ K and 11.5 K, but is absent for 16 K. Fits to Gaussian lineshapes find that the magnetic-Bragg peaks are centered at $h = -0.3443(1)$ r.l.u. (reciprocal lattice units) and $h = -0.3554(1)$ r.l.u. for 5.5 and 11.5 K, respectively. The much stronger peak appearing at $h = -\frac{1}{3}$ r.l.u. in all three datasets is from the $(7, \bar{1}, 6)$ structural (electronic) Bragg peak and arises from diffraction of x-rays with $\frac{1}{3}$ the wavelength of those corresponding to $E = 7.610$ keV. This was verified by observing its negligble response to the insertion of x-ray attenuators which have a much greater effect on 7.610 keV x rays than on 22.830 keV x rays.

A more detailed temperature dependence of the $(2+\tau_h, \bar{\tau}_h, 2)$ magnetic-Bragg peak is given in Fig. 8(c). The sample was realigned at each temperature before making a $(2-h, h, 2)$ scan. Fits using a Gaussian lineshape find that the full width at half maximum of the $(2+\tau_h, \bar{\tau}_h, 2)$ peak does not change with decreasing temperature but that the center moves towards $(2\,0\,2)$. This is shown by the black dots in Fig. 8(c) and the plot in Fig. 9. The magnetic-Bragg peaks appear at $T_{N1} \approx 14$ K and there is a jump in τ_h at $T_{N3} \approx 11$ K, which is further evidence for the first order nature of the transition at T_{N3}, which was suggested by the derivatives of $R/R_{300\,K}$ and MT/H data in Fig. 4. The temperature dependence of τ between ≈ 11 and 14 K and its incommensurate value are consistent with the analysis of the Mössbauer data. The XRMS data indicate that τ_h locks into $\tau_h = 0.3443(1)$ at low temperature which is not an obviously commensurate value. Data in Figs. 8(b) and 8(c) show that the center of the third-order $(7, \bar{1}, 6)$ charge-Bragg peak does not change between 5.5 and 16 K which gives an excellent reference point confirming that the magnetic peak is not at a commensurate position and validate the precision and accuracy we claim for the XRMS $\tau_h(T)$ data. Future experiments like neutron diffraction or polarized XRMS are needed to determine the further details of the magnetic structure of $EuIn_2$.

It would be useful to study the magnetic interactions in $EuIn_2$, as multiple closely spaced transitions indicates multiple phases with similar energy, that could be arising from competing interactions. The nature of the competing magnetic interactions and the role of the triangular lattice in facilitating

of repressing those would be of interest. $EuIn_2$ forms an excellent material candidate to explore these questions, as many other widely studied hexagonal or trigonal Eu^{2+} containing compounds, with a triangular lattice of divalent Eu ions ($EuMg_2Bi_2$ [10], $EuSn_2As_2$ [46], $EuAl_2Ge_2$ [13], $EuCd_2As_2$ [47]) tend to order in AFM-A structure, with ferromagnetic layers of Eu^{2+} ions coupled antiferromagnetically accross the layers, thereby avoiding the possibility of the existence of geometric frustration.

IV. CONCLUSION

In summary, we have synthesized single crystals of $EuIn_2$, which is a magnetic topological semimetal candidate according to DFT calculations. $EuIn_2$ undergoes three magnetic transitions with decreasing temperatures, between 10–15 K. Clear signatures of the transitions are observed both in magnetic susceptibility and electrical resistivity measurements. Furthermore, Mössbauer spectroscopy measurements suggest a likely incommensurate ground state, evolving into a complicated modulated moment order on warming, which eventually turns into a sinusoidally modulated order before turning paramagnetic above T_{N1}. XRMS data indicate antiferromagnetic ordering with an incommensurate propagation vector, which changes with decreasing temperatures below T_{N1}. The propagation vector locks in to an incommensurate value below T_{N3}, through a first-order transitionlike jump. Future work further characterizing the magnetic ordering and magnetic phases transitions as a function of field or pressure should provide more insight into the energetics behind the closely lying magnetic phases. Further experiments to directly measure the band structure and probe the existence of topologically nontrivial phases and their evolution with magnetic phase transitions are promising as well.

ACKNOWLEDGMENTS

B.K. would like to thank Sergey L. Bud'ko for his guidance and useful discussions. Work at the Ames National Laboratory was supported by the U.S. Department of Energy, Office of Science, Basic Energy Sciences, Materials Sciences and Engineering Division. The Ames National Laboratory is operated for the U.S. Department of Energy by Iowa State University under Contract No. DEAC0207CH11358. B.K., P.C.C., S.X.M.R., L.-L.W., B.G.U., and R.J.M. were supported by the Center for the Advancement of Topological Semimetals, an Energy Frontier Research Center funded by the U.S. DOE, Office of Basic Energy Sciences. A portion of this research used resources at the Advanced Photon Source, which is a U.S. DOE SC User Facility operated by Argonne National Laboratory under Contract No. DE-AC02-06CH11357. Financial support for this work was provided by Fonds Québécois de la Recherche sur la Nature et les Technologies, and the Natural Sciences and Engineering Research Council (NSERC) Canada. Some of this work was carried out, while D.H.R. was on sabbatical at Iowa State University and their generous support during this visit is gratefully acknowledged.

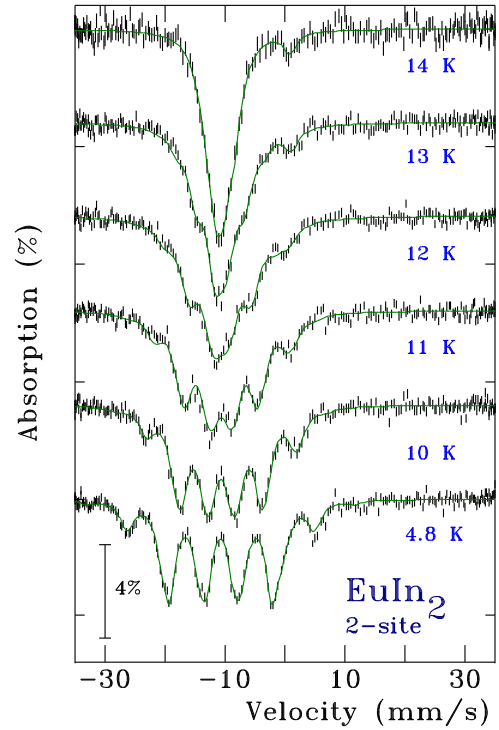

FIG. 10. ^{151}Eu Mössbauer spectra of $EuIn_2$ at various temperatures as we cool down from 14 to 4.8 K. The green solid lines are fit using a two site fit, one magnetic with a temperature-dependent B_{hf}, and the other with no magnetic splitting.

APPENDIX

A. Powder x-ray diffraction

Table I shows the lattice parameters and atomic parameters obtained from the Rietveld refinement of the ambient temperature powder x-ray diffraction data. The crystallographic parameters were obtained from a Rietveld refinement using GSAS-II software, [28] from data that was collected on ground crystals using a Rigaku Miniflex diffractometer inside a nitrogen filled glovebox, with Cu K_α radiation, at room temperature. The cif file (ICSD-103398) from Ref. [22], obtained from the Inorganic Crystal Structure Database (ICSD) [48] was used as the starting point for refinements. We found that it was necessary to include a correction for surface roughness (likely due to the rather absorbing heavy elements present [49]) in order to avoid anomalously low thermal parameters.

B. Mössbauer spectroscopy

In this section, we describe in detail the two models used to fit the Mössbauer spectroscopy data. Figure 10 shows the ^{151}Eu Mössbauer spectra of $EuIn_2$ at low temperatures. At the lowest measured temperature of 4.8 K, the spectrum shows a well-split magnetic pattern, typical for a magnetically ordered Eu^{2+} compound. As we increase the temperature, the spectra evolve, with the absorption lines getting broader and the relative intensities changing. The spectra become qualitatively different, with inner lines having higher intensities than the outer lines, leading to the characteristic shape between 11–13 K. The spectra then evolve to a single Eu^{2+} line at

TABLE I. The lattice parameters obtained from Rietveld refinements of the powder x-ray diffraction measured at room temperature on the ground crystals of $EuIn_2$. The refinement had a weighted R factor $wR = 5.08\%$ and goodness of fit 1.58. Refined atom parameters including atomic positions and thermal parameters (U_{iso}) are also shown. The two sites were assumed to be fully occupied.

		space group	$P6_3/mmc$			
		$a = b =$	4.9814(2) Å			
		$c =$	7.8713(2) Å			
		$\alpha = \beta =$	90°			
		$\gamma =$	120°			
Site	Wyckoff position	Symmetry	x	y	z	U_{iso} (Å^2)
Eu	$2b$	$-6m2$	0	0	1/4	0.0017(7)
In	$4f$	$3m$	1/3	2/3	0.4544(2)	0.0056(6)

14 K, typical for the paramagnetic phase. One simple way to fit the increased intensities at the center is by including a nonmagnetic component into the fits. This is achieved in the two-site fits shown in Fig. 10 as solid green lines. Here, we assume two Eu sites, one with a temperature-dependent hyperfine field resulting from magnetic ordering and another nonmagnetic. Although this model appears to fit the data satisfactorily, the likeliness of such a situation is very low. Increasing linewidths with increasing temperature, indicating a distribution of fields is clearly seen in the lower panel of Fig. 11. The upper panel shows a nonmagnetic Eu site existing above 9 K, whose fraction reaches up to 30% around 13 K. The existence of such a large fraction of nonmagnetic phase is hard to explain as we clearly see signatures of magnetic transitions in bulk measurements like magnetic susceptibility and resistivity.

The physically unreasonable results of the two-site fit call for a different possible explanation or model for this behavior. One way to model the particular shape of the Mössbauer

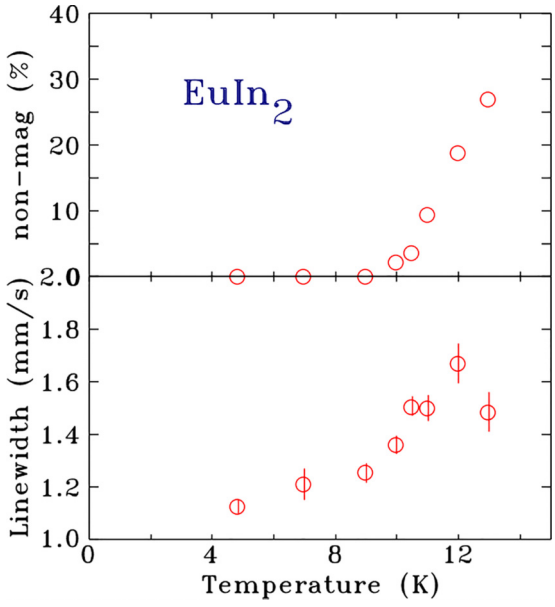

FIG. 11. The temperature dependence of the parameters obtained form the two site fit of the ^{151}Eu Mössbauer spectra of $EuIn_2$. Top panel shows the fraction of non magnetic sites in percentage. Bottom panel shows the increasing linewidths with increasing temperature, obtained from the fits, indicating a distribution of hyperfine fields.

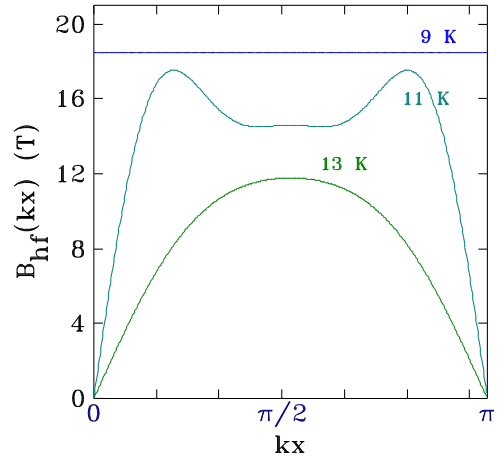

FIG. 12. The modulation of the hyperfine field B_{hf} with kx, for the Fourier components obtained from fitting the spectra at $T = 9$, 11, and 13 K. At 13 K, the modulation is purely sinusoidal, which then evolves with higher harmonics appearing, as shown for 11 K. At 9 K, there is a single hyperfine field, indicating a squared up, but not necessarily *commensurate*, ordering, at low temperatures.

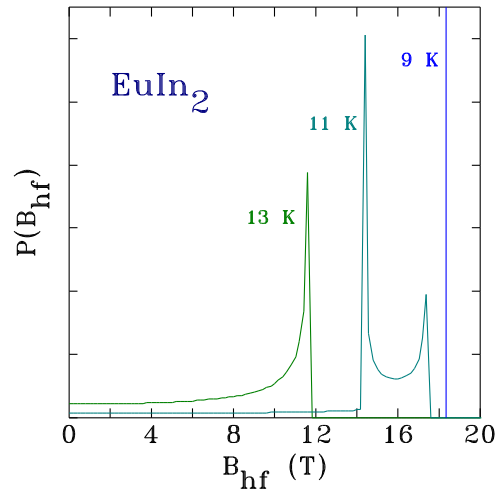

FIG. 13. The probability distributions of the hyperfine field $P(B_{hf})$ versus B_{hf}, for the three different modulations shown in Fig. 12, corresponding to Fourier components from the fits at $T = 9$, 11, and 13 K.

spectra between 11–13 K is by assuming a distribution of hyperfine fields arising from an incommensurate modulation of the magnetic moments [30]. Such a model has been used previously to explain the magnetic ordering in many other Eu compounds [20,31,45]. Details of this model are discussed and fits shown in the main text.

The sequence of fitting the Mössbauer spectra using the modulated model is as follows: Assuming a modulation of the time-averaged Eu^{2+}moments, the hyperfine field at each Eu-site shows a similar modulation as well. This modulation of B_{hf} along the propagation vector is evaluated using Eq. (1) and an initial set of Fourier components Bk_n. Examples of such modulations in B_{hf} versus kx, where x is the distance along k, the propagation vector of Eu-moments ordering, are shown in Fig. 12. The Bk_n values used for generating the plot are those obtained from fitting the spectra at $T =$ 9,11, and 13 K. The probability distribution of the hyperfine fields, $P(B_{\mathrm{hf}})$ versus B_{hf}, is obtained from it, as plotted in Fig. 13. The modulated model spectrum is then calculated by performing a sum of the single hyperfine field spectra (with a constant linewidth of 1.25 mm/s) weighted according to this probability distribution. The result thus obtained is then fitted with the experimental data by a conventional nonlinear least-squares algorithm to adjust the Bk_n values. The temperature dependence of different Bk_n values obtained from fitting the spectra at different temperatures is plotted in Fig. 7(b) and discussed in the main text. An average hyperfine field was also calculated at each temperature as a simple weighted sum of the fitted probability distribution, and those values are plotted in Fig. 7(a).

[1] D. Hsieh, D. Qian, L. Wray, Y. Xia, Y. S. Hor, R. J. Cava, and M. Z. Hasan, Nature (London) **452**, 970 (2008).
[2] M. Z. Hasan and C. L. Kane, Rev. Mod. Phys. **82**, 3045 (2010).
[3] A. A. Burkov and L. Balents, Phys. Rev. Lett. **107**, 127205 (2011).
[4] A. Burkov, Nat. Mater. **15**, 1145 (2016).
[5] C.-K. Chiu, J. C. Y. Teo, A. P. Schnyder, and S. Ryu, Rev. Mod. Phys. **88**, 035005 (2016).
[6] B. Yan and C. Felser, Annu. Rev. Condens. Matter Phys. **8**, 337 (2017).
[7] N. P. Armitage, E. J. Mele, and A. Vishwanath, Rev. Mod. Phys. **90**, 015001 (2018).
[8] Y. Tokura, K. Yasuda, and A. Tsukazaki, Nat. Rev. Phys. **1**, 126 (2019).
[9] N. J. Ghimire, R. L. Dally, L. Poudel, D. C. Jones, D. Michel, N. T. Magar, M. Bleuel, M. A. McGuire, J. S. Jiang, J. F. Mitchell, J. W. Lynn, and I. I. Mazin, Sci. Adv. **6**, eabe2680 (2020).
[10] M. Marshall, I. Pletikosić, M. Yahyavi, H.-J. Tien, T.-R. Chang, H. Cao, and W. Xie, J. Appl. Phys. **129**, 035106 (2021).
[11] S. X. M. Riberolles, T. V. Trevisan, B. Kuthanazhi, T. W. Heitmann, F. Ye, D. C. Johnston, S. L. Bud'ko, D. H. Ryan, P. C. Canfield, A. Kreyssig, A. Vishwanath, R. J. McQueeney, L. L. Wang, P. P. Orth, and B. G. Ueland, Nat. Commun. **12**, 999 (2021).
[12] S. X. M. Riberolles, T. J. Slade, D. L. Abernathy, G. E. Granroth, B. Li, Y. Lee, P. C. Canfield, B. G. Ueland, L. Ke, and R. J. McQueeney, Phys. Rev. X **12**, 021043 (2022).
[13] S. Pakhira, A. K. Kundu, F. Islam, M. A. Tanatar, T. Roy, T. Heitmann, T. Yilmaz, E. Vescovo, M. Tsujikawa, M. Shirai, R. Prozorov, D. Vaknin, and D. C. Johnston, Phys. Rev. B **107**, 134439 (2023).
[14] A. F. May, M. A. McGuire, and B. C. Sales, Phys. Rev. B **90**, 075109 (2014).
[15] J.-R. Soh, P. Manuel, N. M. B. Schröter, C. J. Yi, F. Orlandi, Y. G. Shi, D. Prabhakaran, and A. T. Boothroyd, Phys. Rev. B **100**, 174406 (2019).
[16] N. H. Jo, B. Kuthanazhi, Y. Wu, E. Timmons, T.-H. Kim, L. Zhou, L.-L. Wang, B. G. Ueland, A. Palasyuk, D. H. Ryan, R. J. McQueeney, K. Lee, B. Schrunk, A. A. Burkov, R. Prozorov, S. L. Bud'ko, A. Kaminski, and P. C. Canfield, Phys. Rev. B **101**, 140402(R) (2020).
[17] S. Pakhira, M. A. Tanatar, and D. C. Johnston, Phys. Rev. B **101**, 214407 (2020).
[18] L.-L. Wang, H. C. Po, R.-J. Slager, and A. Vishwanath, Phys. Rev. B **104**, 165107 (2021).
[19] E. Gati, S. L. Bud'ko, L.-L. Wang, A. Valadkhani, R. Gupta, B. Kuthanazhi, L. Xiang, J. M. Wilde, A. Sapkota, Z. Guguchia, R. Khasanov, R. Valentí, and P. C. Canfield, Phys. Rev. B **104**, 155124 (2021).
[20] N. S. Sangeetha, S. Pakhira, D. H. Ryan, V. Smetana, A.-V. Mudring, and D. C. Johnston, Phys. Rev. Mater. **4**, 084407 (2020).
[21] D. G. Franco and C. Geibel, Phys. Rev. B **104**, 054416 (2021).
[22] A. Iandelli, Zeitschrift anorg allge chemie **330**, 221 (1964).
[23] S. P. Yatsenko, V. M. Zolotarev, and E. G. Fedorova, Russian Metallurgy **2**, 168 (1983).
[24] P. C. Canfield and Z. Fisk, Philos. Mag. B **65**, 1117 (1992).
[25] P. C. Canfield, T. Kong, U. S. Kaluarachchi, and N. H. Jo, Philos. Mag. **96**, 84 (2016).
[26] P. C. Canfield, Rep. Prog. Phys. **83**, 016501 (2020).
[27] H. Okamoto, in *Eu-In (Europium-indium), ASM Alloy Phase Diagrams Database*, edited by P. Villars, H. Okamoto, and K. Cenzual (ASM International, Materials Park, OH, 2016).
[28] B. H. Toby and R. B. Von Dreele, J. Appl. Crystallogr. **46**, 544 (2013).
[29] C. J. Voyer and D. H. Ryan, Hyperfine Interact. **170**, 91 (2006).
[30] P. Bonville, J. A. Hodges, M. Shirakawa, M. Kasaya, and D. Schmitt, Eur. Phys. J. B **21**, 349 (2001).
[31] A. Maurya, P. Bonville, A. Thamizhavel, and S. K. Dhar, J. Phys.: Condens. Matter **26**, 216001 (2014).
[32] V. A. Solé, E. Papillon, M. Cotte, P. Walter, and J. Susini, Spectrochim. Acta Part B: Atomic Spectrosc. **62**, 63 (2007).
[33] P. Hohenberg and W. Kohn, Phys. Rev. **136**, B864 (1964).
[34] W. Kohn and L. J. Sham, Phys. Rev. **140**, A1133 (1965).
[35] J. P. Perdew, K. Burke, and M. Ernzerhof, Phys. Rev. Lett. **77**, 3865 (1996).
[36] G. Kresse and J. Furthmüller, Phys. Rev. B **54**, 11169 (1996).
[37] G. Kresse and J. Furthmüller, Comput. Mater. Sci. **6**, 15 (1996).
[38] P. E. Blöchl, Phys. Rev. B **50**, 17953 (1994).

[39] H. J. Monkhorst and J. D. Pack, Phys. Rev. B **13**, 5188 (1976).
[40] M. E. Fisher, Philos. Mag. **7**, 1731 (1962).
[41] M. E. Fisher and J. S. Langer, Phys. Rev. Lett. **20**, 665 (1968).
[42] R. W. Shaw, D. E. Mapother, and D. C. Hopkins, Phys. Rev. **120**, 88 (1960).
[43] G. J. Long and F. Grandjean (eds.), *Mössbauer Spectroscopy Applied to Inorganic Chemistry*, Modern Inorganic Chemistry, Vol. 3 (Plenum Press, NY, 1989).
[44] N. Kumar, S. K. Dhar, A. Thamizhavel, P. Bonville, and P. Manfrinetti, Phys. Rev. B **81**, 144414 (2010).
[45] D. H. Ryan, A. Legros, O. Niehaus, R. Pöttgen, J. M. Cadogan, and R. Flacau, J. Appl. Phys. **117**, 17D108 (2015).
[46] S. Pakhira, M. A. Tanatar, T. Heitmann, D. Vaknin, and D. C. Johnston, Phys. Rev. B **104**, 174427 (2021).
[47] M. C. Rahn, J.-R. Soh, S. Francoual, L. S. I. Veiga, J. Strempfer, J. Mardegan, D. Y. Yan, Y. F. Guo, Y. G. Shi, and A. T. Boothroyd, Phys. Rev. B **97**, 214422 (2018).
[48] D. Zagorac, H. Müller, S. Ruehl, J. Zagorac, and S. Rehme, J. Appl. Crystallogr. **52**, 918 (2019).
[49] L. B. McCusker, R. B. Von Dreele, D. E. Cox, D. Louër, and P. Scardi, J. Appl. Crystallogr. **32**, 36 (1999).